POLITECNICO DI TORINO
Repository ISTITUZIONALE

In-cylinder pressure-based direct techniques and time frequency analysis for combustion diagnostics in IC engines

Original
In-cylinder pressure-based direct techniques and time frequency analysis for combustion diagnostics in IC engines / D'Ambrosio, Stefano; Ferrari, Alessandro; Galleani, Lorenzo. - In: ENERGY CONVERSION AND MANAGEMENT. - ISSN 0196-8904. - ELETTRONICO. - 99:(2015), pp. 299-312. [10.1016/j.enconman.2015.03.080]

Availability:
This version is available at: 11583/2628094 since: 2016-01-13T17:21:27Z

Publisher:
Elsevier Ltd

Published
DOI:10.1016/j.enconman.2015.03.080

Terms of use:

This article is made available under terms and conditions as specified in the corresponding bibliographic description in the repository

Publisher copyright
Elsevier preprint/submitted version

Preprint (submitted version) of an article published in ENERGY CONVERSION AND MANAGEMENT © 2015, http://doi.org/10.1016/j.enconman.2015.03.080

(Article begins on next page)

19 April 2024

IN-CYLINDER PRESSURE-BASED DIRECT TECHNIQUES AND TIME FREQUENCY ANALYSIS FOR COMBUSTION DIAGNOSTICS IN IC ENGINES.

d'Ambrosio, S[1]. , Ferrari, A.[1], and Galleani, L.[2]*

[1] Energy Department – Politecnico di Torino
[2] Department of Electronics and Telecommunications – Politecnico di Torino
C.so Duca degli Abruzzi, 24, 10129, Torino, Italy.

ABSTRACT

In-cylinder pressure measurement and analysis has historically been a key tool for off-line combustion diagnosis in internal combustion engines, but online applications for real-time condition monitoring and combustion management have recently become popular. The present investigation presents and compares different low computing-cost in-cylinder pressure based methods for the analyses of the main features of combustion, that is, the start of combustion, the end of combustion and the crankshaft angle that responds to half of the overall burned mass. The instantaneous pressure in the combustion chamber has been used as an input datum for the described analytical procedures and it has been measured by means of a standard piezoelectric transducer.

Traditional pressure-based techniques have been shown to be able to predict the burned mass fraction time history more accurately in spark ignition engines than in diesel engines. The most suitable pressure-based techniques for both spark ignition and compression ignition engines have been chosen on the basis of the available experimental data. Time-frequency analysis has also been applied to the analysis of diesel combustion, which is richer in events than spark ignited combustion. Time frequency algorithms for the calculation of the mean instantaneous frequency are computationally efficient, allow the main events of the diesel combustion to be identified and provide the greatest benefits in the presence of multiple injection events. These algorithms can be optimized and applied to onboard diagnostics tools designed for real control, but can also be used as an advanced validation tool for refined combustion models.

The presented results on the pressure-based techniques, including a time frequency analysis, have been compared with the numerical outcomes from previously developed two- and three- zone thermodynamic combustion models.

Keywords: combustion; in-cylinder pressure; time frequency analysis.

Highlights:

- Direct pressure-based techniques have been applied successfully to spark-ignition engines.

* Corresponding author e-mail address: alessandro.ferrari@polito.it. Phone: +390110904426.

- The burned mass fraction of pressure-based techniques has been compared with that of 2- and 3-zone combustion models.
- The time frequency analysis has been employed to simulate complex diesel combustion events.

1. INTRODUCTION

Since the invention of internal combustion (IC) engines, the measured time history of the in-cylinder pressure has been the principal diagnostic tool for experimenters. The following parameters can be determined through cylinder pressure analysis: peak pressure and maximum pressure gradient, indicated mean effective pressure, pumping mean effective pressure, burn duration, the shape of heat release, and regularity of combustion. The accuracy of the results on one hand depends on the accuracy of each component of the measuring chain, and on the other hand on the correct processing of the pressure signal. [1]. One of the main features of pressure analysis was its simplicity when the available computational power was low. A heat release model that still maintains simplicity is described in [2], even though this model is also capable of considering important effects, such as heat transfer, crevice flow and fuel injection. In recent years, pressure measurement, by means of highly performing transducers, has still represented one of the most important key parameters for detailed engine studies and diagnosis. The demand for prompt engine control requires the real-time analysis of pressure signals for different purposes. A new method that is able to resolve dynamic knock intensity related to each individual engine cycle, is reported in [3]. The in-cylinder pressure can also be used to obtain a refined closed-loop function in order to control the low temperature combustion mode in Euro 6-compliant diesel engines under steady-state and transient conditions [4]. Furthermore, the instantaneous in-cylinder pressure signal, during the compression stroke, can be used as an alternative to the air mass flow measurement in either naturally aspirated spark ignition or turbocharged diesel engines. This could avoid the need to install an air mass flow sensor, or could provide an improved exhaust gas recirculation (EGR) estimate, if the proposed method is used together with an air mass flow sensor [5]. However, digital filtering must be applied if high quality results are required: the selection of the proper cut-off frequency of a low-pass filter to remove noise related to measurement is mandatory to preserve only physically meaningful information for a reliable heat release analysis on a cycle basis [6]. In order to reduce the computational power for real time-applications, an algorithm that uses the difference pressure instead of the in-cylinder pressure for the calculation of IMEP and MFB50 was developed in [7].

The in-cylinder pressure time history is universally measured using piezoelectric pressure transducers, due to their highly dynamic behavior. However, a piezoelectric sensor only provides the pressure variation with respect to a reference measurement, that is, only a relative value can be measured. The relative pressure has to be referenced to a known value by means of a pegging procedure in order to obtain an absolute value [8]. An accurate pegging method consists of the

installation of a fast-response piezoresistive pressure transducer that is capable of measuring the absolute pressure in the intake manifold or runner. The cylinder pressure, measured by the piezoelectric transducer at the induction process bottom dead center (*BDC*), is set equal to the absolute pressure level at the intake manifold, which is calculated as a time average value of the piezoresistive transducer trace over a certain interval. Furthermore, a direct and reliable measurement of the compression top dead center (*TDC*) position and of the thermodynamic loss angle are necessary to obtain an accurate phasing of the pressure signal with the crank angle [9] and thus to achieve meaningful thermodynamic results from the pressure measurement. In fact, as far as the *imep* evaluation is concerned, an erroneous adjustment of the *TDC* reference position has been recognized to be a major error source: an uncertainty of 1° *CA* is expected to provide a change of up to 10% in the calculated value of the *imep* from the pressure-volume indicated diagram [10]. The effects that crank angle phasing errors can have on the heat release rate and mass fraction burnt have not been clearly defined and quantified [11]. Finally, the measurement noise should be removed from the pressure signal by means of a numerical treatment, which is usually applied after the data have been averaged over several consecutive cycles. Several different methods can be used for this numerical treatment, including fast Fourier transform filters, windowing filters and smoothing splines [6]. A derivative pressure signal coming directly from the pressure transducer is sometimes used without a pressure amplifier [12]. Particular attention has to be paid to filtering and smoothing operations because the pressure fluctuations, which are softened by the filters or altered by the interpolating splines, can contain important information for the detection of combustion [13]. A properly processed pressure signal can be used to provide an evaluation of the main combustion features, either by means of the direct elaboration of the pressure measurement or by means of an indirect heat release analysis, which applies the first law of thermodynamics to the chamber contents on the basis of the in-cylinder pressure time history [14]. Both of these approaches allow the mass fraction of the fuel that has burnt (x_b) to be estimated as a function of time, but the former assumes that x_b is related to the pressures of the fired and unfired cycles rather than to the fuel-released chemical energy [15].

The most important events related to combustion are the start of combustion (*SOC*), end of combustion (*EOC*) and the angular position at which half of the fuel has burnt (*MFB50* is the crankshaft angle that corresponds to x_b=0.5). Combustion duration can easily be expressed as the difference between the *EOC* and *SOC* angles, but sometimes an angular distance between 10% and 90% of x_b is used as an indicator of the combustion period.

One of the first applications of the measured pressure signal used to perform the direct diagnosis of combustion was illustrated by Marvin in [16]. Ideal compression and expansion phases were considered as simple polytropic evolutions, and the crankshaft angles at which the actual pressure starts to differ from the ideal compression and the straight expansion lines in a double logarithmic pressure-volume plane were considered as the *SOC* and *EOC* angles, respectively [17].

These can also be evaluated considering the inflection points in the diagrams of the specific heat ratio during the closed part of the cycle [18].

Marvin's graphical method was analytically developed and experimentally validated by Rassweiler and Withrow (*RW*) in [19]. Their analysis pointed out that the cylinder pressure pattern also depends on the changes in the volume of the combustion chamber, because of the piston motion, on the heat transfer to the chamber walls and on the mass leakages through the piston crevices, in addition to the influence exerted by combustion. The effects of volume change, heat transfer, and mass loss [2] were isolated and analytical formulas were proposed to calculate the *SOC*, the *EOC* and the burned mass fraction [20]. A refined alternative procedure to that of Rassweiler and Withrow has been developed by McCuiston, Lavoie and Kaufmann (*MLK*) [21] on the basis of the pressure and the in-cylinder volume time histories. This procedure works efficiently for gasoline combustion and hypothesizes that the mass of the burned gas is proportional to the pV^{γ} quantity, where γ is the constant pressure-to-constant volume specific heat ratio. The *SOC*, *EOC* and the x_b curve can easily be determined.

Indirect heat release analyses were developed later than direct pressure-based techniques and they stemmed from the application of the first law of thermodynamics. They have been used to develop ordinary differential equation models of combustion that allow the evaluation of the heat release rate (*HRR*), from which the burned mass fraction can then be worked out. Single-zone models define the thermodynamic state of the cylinder charge, in terms of average properties of a pure phase [2], but do not distinguish between burned and unburned gases. In simpler models, heat transfer and crevices are neglected and an apparent *HRR*, also referred to as net *HRR*, is calculated [22] as a function of the measured pressures and volumes. Considering a heat transfer model [23], and also taking the crevice volume into account [2], the gross *HRR* due to the chemical energy released by the fuel is obtained, and a more accurate x_b time distribution can be evaluated. The correlation proposed by Woschni [24], and validated on a huge number of experimental tests, is widely adopted for the simulation of the heat transfer coefficient, but some constant parameters of this correlation have to be tailored on to the basis of the considered engine layout and working conditions [25]. The combustion efficiency measured from exhaust emissions can be used to calibrate these constant parameters, and a physically-consistent final predicted value of x_b [17] can thus be obtained from the combustion model.

Two-zone models, in which one zone represents the unburned mixture upstream of the flame, and the other simulates the burned mixture downstream from the flame [25], are more refined and complex than single zone models. The grade of complexity of the model is further increased in the multi-zone approach [26], in which the burned gases are simulated by means of different zones, even though this modeling strategy can also be considered reasonable when an enhanced prediction of engine-out emissions is required. *SOC* is generally easier to determine than *EOC,* because the latter is less repetitive, due to the inherent difficulty in its localization and the arbitrariness of its practical definition [13]. The energy

conservation equation of the unburned gas mass can be considered for *SOC* evaluation in the context of the *HRR* analysis. Since changes in the sensible internal energy of the charge during the compression phase are only due to work and heat exchanges with the combustion chamber walls, *SOC* can ideally be evaluated as the instant at which the energy conservation mass of the unburned gas fails to be verified [27]. For a practical and effective evaluation, a threshold can be set on the value of the x_b, e.g. 1%. However, the necessity of larger threshold values in the *SOC* identification process has already been pointed out [28], due to uncertainties that are related to pressure and volume measurements and to the large dispersion of this parameter if ensemble-averaged pressure data are considered. *EOC* can be evaluated in the *HRR* analysis as the crank angle at which x_b reaches a certain threshold (e.g. 0.99) for single-zone models [29], or as the crank angle at which the theoretical x_b reaches the experimental combustion efficiency measured from emissions for two- and multi-zone models. Otherwise, since *HRR* expresses the rate at which the fuel releases its chemical energy, a correspondence can be set between *EOC* and the crank angle at which the *HRR* falls below a minimum threshold, e.g. 3% of the maximum *HRR*.

Since accurate heat release analyses are rather complex and time consuming, the direct utilization of the in-cylinder pressure is often the preferred option in order to obtain fast, although approximate, results with the possibility of real-time calculation. Some pressure-based direct approaches, for instance, the polytropic volume method [30], have the aim of maintaining the simplicity and the small computational efforts of the *RW* method, but have been developed to overcome its inherent limitations [31]. Another example is that of the Pressure-Ratio Management (*PRM*) method, developed for naturally aspired spark-ignition engines, which involves the calculation of the ratio of the fired pressure to the corresponding motored in-cylinder pressure at each crank angle [32]. This methodology, combined with optical analysis, has also been applied to combustion investigation in [33].

The simple *PRM* approach has been modified to obtain the Pressure Departure Ratio (*PDR*) algorithm [32], which is more suitable for diesel propulsion systems. In the *PDR* model, the ratio of the fired to the motored pressure is corrected by means of two constants, which should be calibrated for each engine setup. The *PDR* algorithm is able to predict *MFB50* with adequate accuracy and is suitable for real-time applications, without any preliminary treatment for the pressure data, unlike apparent *HRR* analyses, in which the derivative term of the pressure can be affected negatively by high measurement noise, and moving average techniques should be applied to the original signal in order to remove spurious high frequency oscillations from the *HRR* trace [34]. Other pressure-based direct methods for the real-time calculation of the main combustion parameters are founded on the pressure-difference apparent heat release analysis [7], in which the difference between the actual pressure and motored pressure (the latter is calculated assuming a polytropic law for the compression phase) is used instead of the in-cylinder pressure, since the heat released by the motored pressure is nil [7]. The advantage of these procedures is that the pressure differences are not affected by pegging uncertainties.

A simple pressure-based direct procedure, which is founded on the *MLK* technique, relates the *EOC* to the angle at which quantity $pV^{1.15}$ reaches a maximum value [11]. The calculation is started 10 *CA ATDC* and continues up to 10 *CA,* before exhaust valve opening by steps of 1 *CA*. *EOC* is set equal to the crank angle that corresponds to the maximum of the $pV^{1.15}$ plus 10°*CA*. A low value of the polytropic index is chosen for the expansion phase (the normally adopted values are around 1.3, which are significantly higher than 1.15) to ensure reliable results, even in the presence of large pressure uncertainties which can make the detection of the maximum point difficult. The addition of 10 *CA* to the angle that corresponds to the maximum of $pV^{1.15}$ allows the low value of the polytropic index to be partly compensated and guarantees complete combustion [11].

The investigation of the derivative of the pressure signal with respect to time has also been proposed for combustion detection. A fourth-order finite difference scheme can be applied to the pressure signal in order to reduce the noise measurement effects in the calculus of the pressure derivative [12]. A sudden increase in the d*p/dt* signal appears at the combustion development stage and this can be used to determine the *SOC*, while *EOC* can be detected on the basis of the attenuation of the oscillations in the pressure derivative time history [13]. Time-frequency analysis of the in-cylinder pressure derivative has recently been applied to detect combustion [13]. This signal processing technique was introduced into the engine field to detect knock and block vibration and for the diagnosis of the injection process [35]. The fundamental idea behind time-frequency analysis is to be able to understand and describe how the spectral content of a signal changes in time, while classical signal analysis usually dealt with time and frequency separately [36]. In general, time-frequency analysis is approached using the spectrogram, which is based on the short-time Fourier transform (*STFT*) concept [37], but many other methods have been proposed and applied [38]. Qualitative criteria of the signal frequency should allow the existence of combustion to be detected, while time information can serve for combustion localization.

In the present work, a comparison has been made between the most popular pressure-based direct methods and single, two-zone and three-zone combustion models; reference has been made to different working conditions for both spark-ignition and compression-ignition *IC* engines. The time frequency analysis and the spectrogram theory have also been applied to both the in-cylinder pressure signal and the difference between fired and motored pressure in diesel engines. The mean instantaneous frequency [39] has been calculated from a home-made tool on the basis of the spectrogram, and this signal allows detailed information on the development and evolution of diesel combustion to be extracted.

2. PRESSURE-BASED DIRECT METHODS FOR COMBUSTION SIMULATION.

Marvin's original work referred to gasoline engines [17]. A typical *p-V* diagram of a naturally-aspired spark-ignition engine (*iV*=2000 cm^3) applied to a passenger car [40] is reported in Fig. 1a (*bmep*=790 kPa, *n*=3300 rpm) and a portion of this diagram is plotted on logarithmic coordinates in Fig. 1b to illustrate the procedure. The dashed line shows actual

in-cylinder pressures measured by a piezoelectric pressure transducer, whereas the ideal Otto combustion is represented by means of a vertical segment. The compression and the expansion phases are represented as polytropic evolutions, according to the $pV^m=const$ law, and they become straight lines plotted with a solid line in the $\log p - \log V$ diagram. Polytropic exponents equal to $m_c \approx 1.34$ and $m_e \approx 1.27$ have been considered for the closer-to-*TDC* portion of the compression and expansion phases, respectively, in line with values in [18]. In [33], the following values are proposed: $m_c=1.35$ and $m_e=1.25$. The crankshaft angles at which the actual pressure starts to differ from the ideal compression and straight expansion lines can be identified as the *SOC* and *EOC* angles, respectively: $SOC \approx 348°\ CA$ and $EOC \approx 414°\ CA$ in Fig. 1b. The combustion duration should be estimated as $\Theta_{comb}=(EOC-SOC)$ and results to be around 66° *CA* for the considered example. Furthermore, Marvin assumed that the pressure rise above the straight compression line was proportional to the mass of burned fuel. Therefore, x_b at a certain point *C* (Fig. 1b) is given roughly by the ratio of length *C'A* to length *AB*. Point *C'* is the projection, on the top dead center line, of point *C*, which belongs to the actual pressure curve. This projection occurs by means of the straight line *C'C*, which is parallel to the polytropic compression straight line when *C* is located between *SOC* and *TDC* ($\theta_{TDC}=360°CA$) and is parallel to the polytropic expansion straight line when *C* is situated between *TDC* and *EOC*.

The burned mass fraction curve, determined according to the Marvin procedure ($x_{b,M}$), is reported in Fig. 2 on the basis of the data given in Fig. 1b and is compared with the x_b distribution obtained using a two-zone combustion diagnostic model (the *RW* method, to which $\Delta p_{comb,RW}$ and $x_{b,RW}$ in Fig. 2 refer, will be discussed in detail later on in this section). The agreement between the Marvin distribution and the theoretical curve of the two-zone model is acceptable, with a difference of $\Delta x_b \approx 2.5\%$ between the two curves at $\theta=400°CA$. The most interesting point of the burned mass fraction profile is its half value ($x_b \approx 0.5$): Fig. 2 shows that the difference is about 1.5°*CA* between the *MFB50* values estimated by means of the two approaches. None of the abovementioned discrepancies between Marvin's method and the two-zone model can be regarded as being only due to the inaccuracy of the Marvin estimation of the burned mass fraction, since the x_b curve of the two-zone model is also affected by some uncertainties, which are primarily due to the calibration procedure of the coefficients of the wall heat transfer model. In general, the less the difference between exponents m_c and m_e, the better the performance of the Marvin method in the calculation of the x_b curve. Marvin's graphical procedure for the evaluation of x_b cannot be extended easily to diesel engines because the Sabathé cycle, which is the general reference for compression ignition engines in passenger cars, also involves a combustion phase at constant pressure.

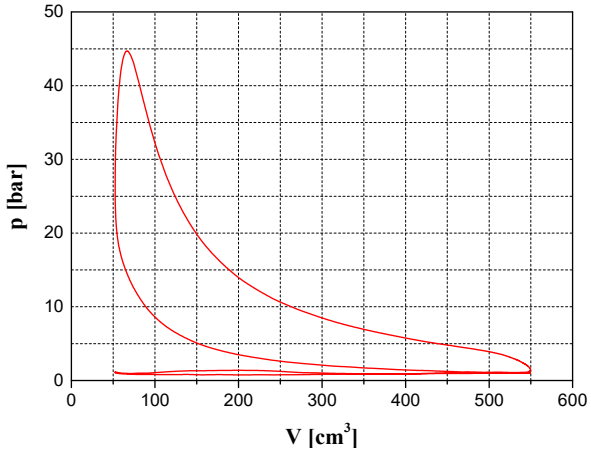

Figure 1a. Indicated *p-V* diagram

(gasoline engine, *bmep*=790 kPa, *n*=3300 rpm)

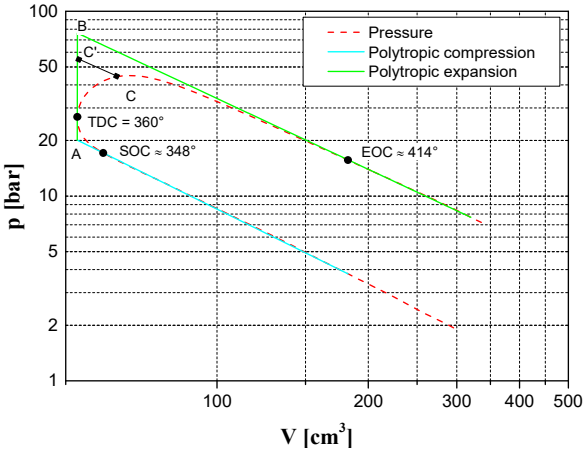

Figure 1b. Enlargement of the indicated diagram in the log*p*-log*V* plane (*bmep*=790 kPa, *n*=3300 rpm).

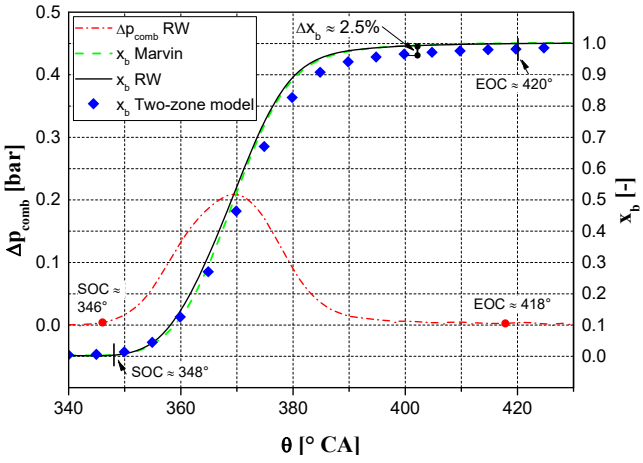

Figure 2. x_b with the Marvin and RW procedures

(gasoline engine, *bmep*=790 kPa, *n*=3300 rpm).

The *RW* method represents a sort of analytical version of Marvin's graphical procedure. It is based on the hypothesis that the changes in the pressure, due to piston motion and the charge-to-wall heat transfer, can be represented by polytropic processes. In this method, the pressure variation during any crank angle increment $\Delta\theta=\theta_i-\theta_{i-1}$ consists of two parts: a pressure rise due to combustion ($\Delta p_{comb,RW}$) and a pressure contribution due to volume change and heat exchanges. The term $\Delta p_{comb,RW}$ can be evaluated as the difference between the actual and polytropic pressures by means of the following formulas, in which the pressure values are measured and the volumes are calculated [19]:

$$\begin{cases} \Delta p_{comb,RW}(\theta_i) = p(\theta_i) - p_{i-1}\left[V_{i-1}/V(\theta_i)\right]^{m_c} & \text{if} \quad \theta \le \theta_{TDC} \\ \Delta p_{comb,RW}(\theta_i) = p(\theta_i) - p_{i-1}\left[V_{i-1}/V(\theta_i)\right]^{m_e} & \text{if} \quad \theta \ge \theta_{TDC} \end{cases} \tag{1}$$

The *SOC* (lower than θ_{TDC}) and the *EOC* (higher than θ_{TDC}) are the maximum and the minimum crankshaft angles, respectively, for which $\Delta p_{comb,RW}$ becomes virtually nil. The fitting of the m_c and m_e polytropic indexes should be carried out by means of a least square technique performed over crank angle intervals of 20°÷50°*CA* just before the start and after the end of combustion, respectively. In particular, m_c can be worked out over an angular interval located just before the high voltage-to-spark instant, whereas m_e can be calculated over an angular window that starts just after the (θ_{max}+10°) angle, where θ_{max} provides the maximum value of quantity pV^{m_e}, this being in line with the procedure outlined in [11]. If reference is made to the data in Fig. 1a (m_e=1.27), one obtains θ_{max}+10°≈430°*CA*, that is, a higher angle than the *EOC* value estimated by means of the Marvin procedure (cf. Fig. 1b).

Figure 2 reports the $\Delta p_{comb,RW}$ versus θ distribution (solid line) that has been calculated by means of Eq. (1) on the basis of the experimental pressure data shown in Fig. 1a. It results that *SOC*≈346°*CA* and *EOC*≈418°*CA,* and these values are very similar to the outcomes of the Marvin graphical procedure.

In the case of the gasoline engine, the elemental combustion heat (δQ_{hrr}) released during the $\Delta\theta$ interval can roughly be modeled as a heat adsorbed during an isochoric evolution, according to the following expression:

$$\delta Q_{hrr} = Mc_v \Delta T_{comb,RW} \tag{2}$$

where M is the constant mixture mass during combustion. The temperature increase ΔT_{comb} can be calculated as

$$\Delta T_{comb,RW} = \frac{\Delta p_{comb,RW} V_{TDC}}{M R} \tag{3}$$

By substituting Eq. (3) in Eq. (2) and taking into account Eq. (1), one obtains:

$$\delta Q_{hrr} \approx \frac{V_{TDC}}{\gamma - 1} \left\{ p(\theta_i) - p_{i-1} \left[V_{i-1} / V(\theta_i) \right]^m \right\} \tag{4}$$

where m can either be m_c or m_e and $\gamma=c_p/c_v$. Parameter γ can be considered as a constant property or expressed as a function of the temperature. Quantity δQ_{hrr} does not include the heat exchanged with the walls, since it has already been included in the m polytropic exponent. In other words, δQ_{hrr} represents the gross heat release, while the apparent or net heat release (δQ_{ahrr}) can be obtained by replacing polytropic index m with factor γ in Eq. (4). Furthermore, heat δQ_{hrr} results to be proportional to $\Delta p_{comb,RW}$, in agreement with Marvin's hypothesis. Therefore, the *RW* algorithm establishes x_b at the end of the i-th interval of amplitude $\Delta\theta$ ($\theta_i=i\Delta\theta$) as [19]

$$x_{b,RW}(\theta_i) = \frac{m_b(\theta_i)}{m_{b,tot}} = \frac{\sum_{k=0}^{i} \Delta p_{comb,RW}(\theta_k)}{\sum_{k=0}^{N} \Delta p_{comb,RW}(\theta_k)} \tag{5}$$

where $m_b(\theta_i)$ denotes the mass of fuel that has already burned at crank angle θ_i, $i=0$ indicates the *SOC* and $N=\Theta_{comb}/\Delta\theta$ designates the *EOC*. As can be seen in Fig.2, the burned mass fraction obtained by means of the *RW* technique is virtually coincident with the curve achieved by means of the Marvin graphical method. It is worth pointing out that if a constant polytropic index equal to $1/2(m_c+m_e)$ was considered for both the compression and expansion phases, as different experimenters have done [8], the pattern of the $x_{b,RW}$ curve in Fig. 2 would not change appreciably. In spite of the evident approximating nature of the *RW* procedure, its accuracy can be considered acceptable and it is still in fact widely used, even for diesel engines, due to its relative simplicity and satisfactory computational efficiency. The criticism inherent to both the Marvin and *RW* methods concerns the choice of the proper angle intervals over which the polytropic exponents are fitted, and the determination of these intervals affects the x_b curve to a great extent.

McCuiston, Lavoie and Kauffmann proposed a relation of the same type as the following one to approximate the x_b curve, on condition that the volume of the burning mixture does not vary significantly during the combustion process:

$$x_{b,MLK} = \frac{pV^m - p_{SOC}V_{SOC}^m}{p_{EOC}V_{EOC}^m - p_{SOC}V_{SOC}^m} \tag{6}$$

where p and V represent the pressure and volume at a certain crank shaft angle θ and p_{SOC}, p_{EOC}, V_{SOC}, and V_{EOC} designate the pressure values and volumes at *SOC* and *EOC*. Unlike Eq. (5), the *MLK* formula also evaluates the volume variations. Eq. (6) can be obtained from the energy equation, provided adequate simplifications are introduced. If crevice volume and blow-by effects are neglected, the heat release equation can be written as

$$\delta q_{hrr} = dx_b H_i = c_v dT + pdv - \delta q_{ht} \tag{7}$$

where v is the specific volume of the mixture, H_i is the lower heating value of the fuel and $\delta q_{ht}=cdT$ represents the heat transfer with the walls, $c=c_v(m-k)/(m-1)$ being the polytropic specific heat for the wall heat exchange. After some arrangements and bearing in mind that $pv=RT$ ($R=c_p-c_v$), Eq. (7) becomes

$$dx_b H_i = \frac{m}{m-1} pdv + \frac{1}{m-1} vdp \tag{8}$$

If the heat exchanged with the walls is overlooked ($\delta q_{ht} \approx 0$), m can be replaced by γ in Eq. (6) and one obtains the original *MLK* formula: the resulting heat release thus becomes equal to the apparent heat release rate (δq_{ahrr}). Apparent heat release rates are usually 10-20% lower than gross heat release rates [20].

Eq. (8) can be rewritten as follows [21]

$$dx_b = \frac{1}{H_i}\frac{d\,(pv^m)}{(m-1)v^{m-1}} = \frac{d\left(y^m\right)}{(m-1)\dfrac{H_i}{p_{SOC}V_{SOC}}\left(\dfrac{V}{V_{SOC}}\right)^{m-1}} \tag{9}$$

where the instantaneous volume V of the combustion chamber and instantaneous pressure have been normalized to their values at *SOC* and quantity y is defined by $y=(V/V_{SOC})(p/p_{SOC})^{1/m}$. Eq. (9) can easily be integrated and, for constant volume combustion, the following expression can then be obtained ($p_{SOC}V_{SOC}=MRT_{SOC}$):

$$y^m(\theta) = 1 + \frac{m-1}{\gamma-1}\frac{H_i}{c_v T_{SOC}}x_b \tag{10}$$

Eq. (10) provides a linear expression for $y^m(\theta)$ as a function of $x_{b,}$ and this expression can also be formulated as [21]

$$y^m = 1 + \left[y^m(\theta_{EOC}) - 1\right]x_b \tag{11}$$

where $y^m(\theta_{EOC})$ corresponds to x_b=1. Eq. (11) can be solved, with respect to $x_{b,}$ in order to obtain the approximate relation for x_b given by Eq. (6). In short, the *MLK* method can be considered a rough application of the heat release analysis and is based on the observation that the heat released by the fuel to the charge in the period from *SOC* to *EOC* is proportional to

$$Q_{hrr} \propto \left(p_{EOC}V_{EOC}^m - p_{SOC}V_{SOC}^m\right) \tag{12}$$

Therefore, the heat released during combustion at angle θ is proportional to pV^m and it can be normalized to the value expressed by Eq. (12) in order to obtain the $x_{b,MLK}$ curve. Although Eq. (6) only holds for isochoric combustion, the inaccuracies in the determination of the angles at which combustion begins and ends are small when the volume does not vary significantly during combustion. Therefore, the simplified *MLK* procedure can be applied to production gasoline engines, but is not suitable for diesel engines in which combustion occurs during a significant change in the V volume.

Figure 3 plots quantity pV^m, divided by a reference value, as a function of θ, for the pressure and volume data reported in Fig. 1a ($m=m_e \approx 1.27$ since most of the combustion develops in the $\theta > \theta_{TDC}$ range for the considered case).

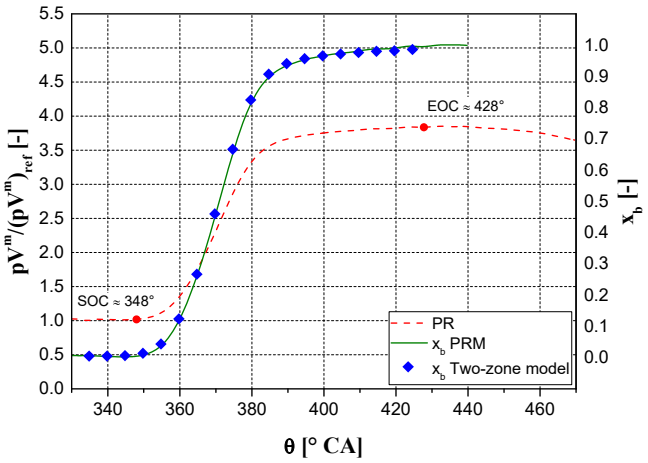

Figure 3. x_b with the *MLK* procedures (gasoline engine, *bmep*=790 kPa, *n*=3300 rpm).

The $pV^{m_e}/(pV^{m_e})_{ref}$ versus θ trace is approximately constant in the compression phase, increases during combustion ($SOC \approx 346°CA$) and is again nearly constant for the remainder of the cycle. This is consistent with the results given in [41], where pV^{γ} is nearly constant during the approximately isentropic processes, while it is not constant during a period of energy release. A maximum point of pV^{m_e} is observable in Fig. 3 at $\theta \approx 424°CA$ and in the *MLK* method this angle corresponds to *EOC*, this being in line with other results concerning the meaning of the maximum value of quantity $pV^{1.15}$ [11]. The x_b time histories predicted by means of the *MLK* technique and the two-zone combustion model have also been reported in Fig. 3. As can be inferred, the $x_{b,MLK}$ curve is virtually coincident with the two-zone model burned mass fraction distribution: the difference between the *MFB50* points of the two curves is less than $0.2°CA$.

The *PRM* algorithm [32] involves the calculation of the ratio between the fired pressure and the corresponding motored cylinder pressure (p_{mot}) at each crank angle. The curve p_{mot} versus θ can be measured experimentally, in the absence of combustion, when the engine is run by an electrical machine, or can be approximated by means of a polytropic evolution (the latter solution is mandatory if the engine is supercharged or turbocharged).

The pressure ratio (*PR*) is defined as [33]

$$PR = \frac{p(\theta)}{p_{mot}(\theta)} \tag{13}$$

This parameter has a unit value before combustion and becomes higher than one during combustion, reaching a maximum value at the end of combustion. The increase in *PR,* with respect to the unit value, is referred to as the modified pressure ratio:

$$MPR(\theta) = \frac{p(\theta)}{p_{mot}(\theta)} - 1 \tag{14}$$

304 The maximum value of *PMR* is reached when *PR* is at a maximum and is called the final *PR* value (*FPR*). It usually
305 ranges from 2.8 to 4.0 and typically occurs at around 55°*CA ATDC* for spark-ignition engines [42]. *FPR* reaches a
306 maximum value for stoichiometric mixtures and decreases as the excess of air, *EGR* or residual gas are increased;
307 therefore, it can also be useful as an indicator of the charge dilution of the combustion system. The *MPR*, once it has been
308 normalized to *FPR*, provides the pressure ratio management procedure for the estimation of x_b [32]:

309
$$x_{b,PRM} = \frac{MPR(\theta)}{FPR} \tag{15}$$

310 Figure 4a plots the $p(\theta)$ and $p_{mot}(\theta)$ signals for the same engine layout and working condition to which Figs. 1-3 refer.
311 The *PR* ratio is reported in Fig. 4b as a function of θ and its maximum value occurs at $\theta \approx 430°CA$, that is, around
312 70°*ATDC*. Furthermore, Fig. 4b shows that the $x_{b,PRM}$ curve is almost coincident with the two-zone model x_b distribution.
313 The direct application of the *PMR* technique to diesel engines can result in a burned mass fraction curve that can differ
314 from the actual cumulative heat release trace, which is calculated by means of a combustion model. In fact, *FPR* occurs
315 towards the exhaust valve opening, due to the much higher compression ratios of the diesel engine, and the *PRM*
316 estimation therefore departs from the actual diesel combustion characteristics, even for single fuel injection schedules.
317 Furthermore, diesel combustion can consist of discrete heat release events because of multiple injection strategies and
318 this represents another main difference from spark ignition engines.

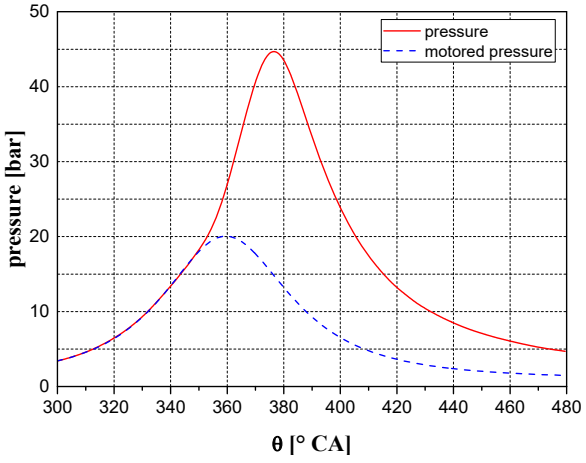

Figure 4a. *p* and p_{mot} angular distributions (gasoline engine, *bmep*=790 kPa, *n*=3300 rpm).

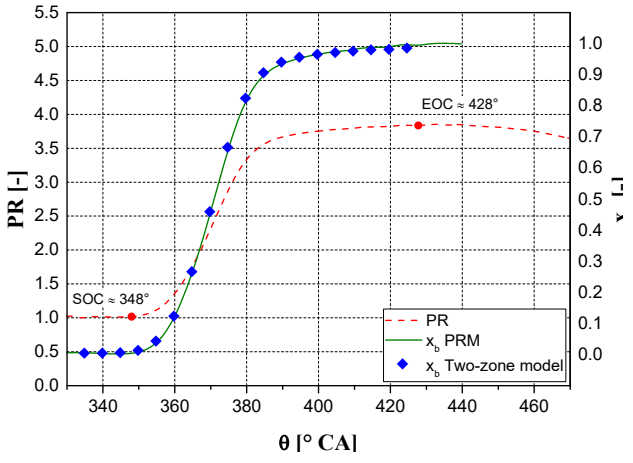

Figure 4b. x_b with the *PRM* procedure (gasoline engine, *bmep*=790 kPa, *n*=3300 rpm).

319 *MPR* in diesel engines is usually substituted by the following pressure departure ratio:

320
$$PDR(\theta) = \frac{p(\theta) + C_1}{p_{mot}(\theta) + C_2} - 1 \tag{16}$$

where C_1 is the fired pressure characterization coefficient and C_2 is the motored pressure characterization coefficient [32]. These empirical coefficients are constant for a given engine configuration. The *PDR* has an almost zero value before combustion and rises to a maximum value (PDR_{max}) which corresponds to *EOC*. An estimate of the mass fraction burnt is obtained by normalizing *PDR* to its maximum value [32]:

$$x_{b,PDR} = \frac{PDR(\theta)}{PDR_{\max}} \tag{17}$$

The C_2 coefficient in Eq. (16) is adjusted so that the $x_{b,PDR}$ trace matches the results of a heat release model as closely as possible: small changes in the C_2 value cause the curve to pivot around a point. The C_1 constant is then selected to shift the pivotal point as close as possible to the actual *MFB50,* because this ensures that small deviations at the extreme ends of the curve will have minimal effects on the prediction of *MFB50*.

Figures 5 and 6 compare the performance of the *RW*, *MLK* and *PRM* methods when applied to the previously considered gasoline engine at *bmep*=440 kPa, *n*=2000 rpm and at *bmep*=620 kPa, *n*=2570 rpm, respectively. The x_b curves, which have been worked out by means of a calibrated two-zone gasoline combustion model, are used as references to evaluate the different pressure-based direct techniques. Furthermore, Fig. 7 shows a comparison of the same abovementioned methods for a spark-ignited *CNG* supercharged engine (*iV*=1242 cm^3) at *bmep*=800 kPa and *n*=3000 rpm. The reference heat release curve has been calculated with a two-zone combustion diagnostic model of the considered *CNG* engine [43].

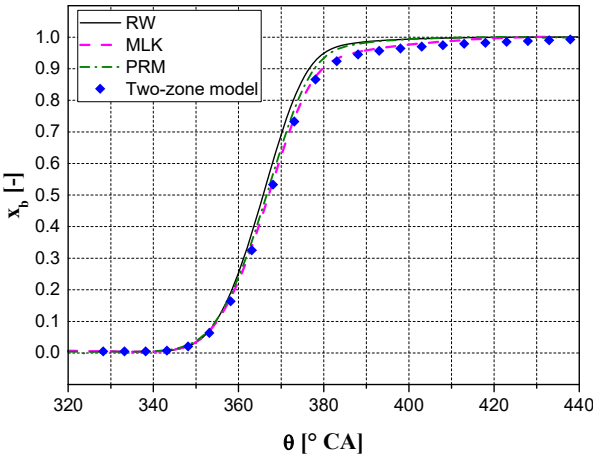

Figure 5. Comparison of the procedures pertaining to x_b (gasoline engine, *bmep*=440 kPa, *n*=2000 rpm).

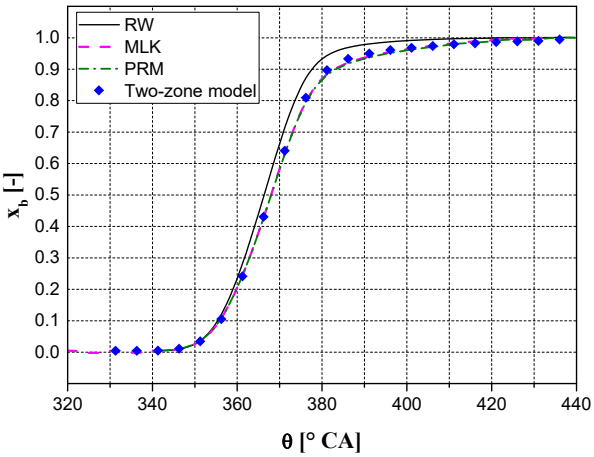

Figure 6. Comparison of the procedures pertaining to x_b (gasoline engine *bmep*=620 kPa, *n*=2570 rpm).

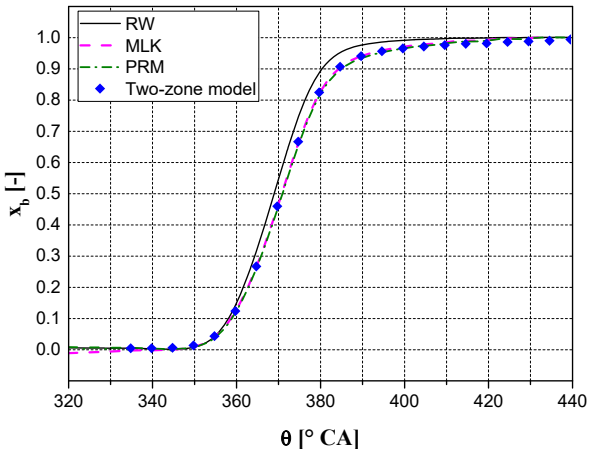

Figure 7. Comparison of the procedures pertaining to x_b (*CNG* engine, *bmep*=800 kPa, *n*=3000 rpm)

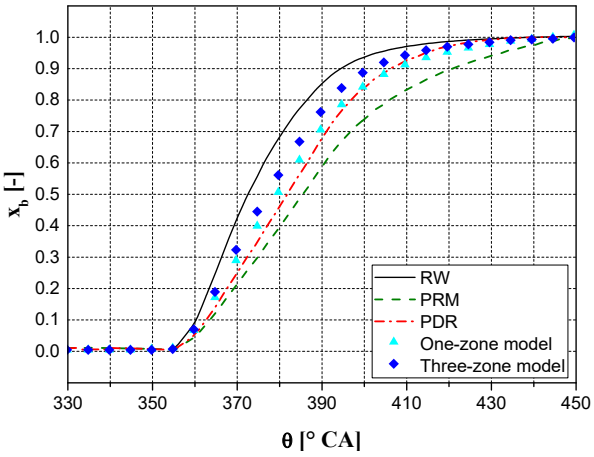

Figure 8. Comparison of the procedures pertaining to x_b (diesel engine, single injection event).

The *MLK* algorithm generally gives results that are virtually coincident with those of two-zone models, although the *PMR* method also guarantees very satisfactory performance. The *MLK* and the *PRM* generally give very similar results because Eqs. (6) and (15) represent the same physical law: in fact, if one divides the numerator and denominator of the right hand member of Eq. (6) by $p_{SOC}V_{SOC}^{m}$, the quantity $p_{SOC}V_{SOC}^{m}/V^{m}$ represents the polytropic pressure (motored pressure) and, as a consequence, Eq. (15) is obtained. The only slight difference between the two techniques can reside in the evaluation of the *EOC*, which coincides with the maximum of p/p_{mot} for the *PMR* procedure and with the maximum of pV^{m} for the *MLK* procedure: these two maxima can occur at different crankshaft angles.

Finally, the data in Figs. 8-10 refer to a twin-stage turbocharged diesel engine (iV=2000 cm^3) [44], fuelled with distinct injection schedules at different *bmep* and *n* conditions. The crankshaft angle based $x_{b,RW}$, $x_{b,PRM}$ and $x_{b,PDR}$ distributions are compared with the x_b traces derived from the application of single-zone and three-zone diagnostic tools for the simulation of diesel combustion. In the calculus of $x_{b,PDR}$, the calibrated values of C_1 and C_2 were set equal to 1.1 and 1.2, respectively, for the turbocharged engine setup tested in the current investigation. These values were selected on the basis of preliminary tests aimed at optimizing the *PDR* method response. As can generally be inferred from Figs. 8-10, the prediction capability of the considered pressure-based techniques becomes worse when passing from spark ignition to compression ignition engines. In particular, the accuracy of the pressure based techniques in the prediction of *SOC*, *EOC* and the x_b trace deteriorates in diesel engines because the combustion evolution becomes more complex, also because of the multiple injection events, and requires more sophisticated approaches. The *PDR* method generally guarantees the best approximation of the x_b distributions obtained by means of the single zone and three-zone models; both the *SOC* and the *EOC* are evaluated with satisfactory accuracy for the single (Fig. 8) and the double injection (Fig. 9) strategies. The *RW* technique gives a better performance than the *PMR* method, which is confirmed to be inadequate for diesel engines, even in the presence of single injection events.

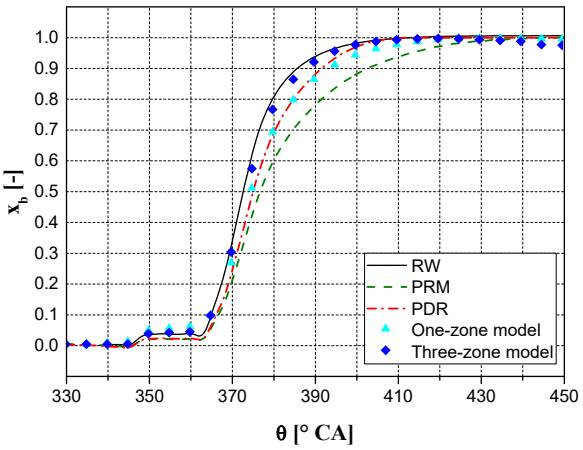

Figure 9. Comparison of the procedures pertaining to x_b (diesel engine, double injection event).

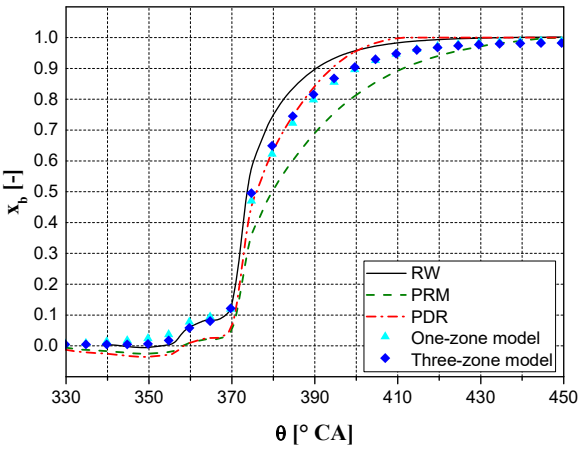

Figure 10. Comparison of the procedures pertaining to x_b (diesel engine, triple injection event).

3. TIME FREQUENCY ANALYSIS

The Fourier transform is suitable for describing stationary phenomena in the frequency domain, but it does not allow transient phenomena that undergo a time evolution to be analyzed. In fact, Fourier transform coefficients represent the time integral of the product between the considered signal and a complex sinusoidal wave, which is determined perfectly in terms of frequency and phase, but is not localized in the time domain [38]. In other words, the *FFT* points out the contribution of the different harmonic terms to the signal, but the time instants at which each frequency component is relevant are not clarified. Instead, time frequency analysis is used to evaluate the changes, with respect to time, in the frequency spectrum of a transient signal *f(t)*. A large number of fast Fourier transforms are realized over different consecutive short time intervals and each *FFT* is referred to the mean instant of the short time interval over which the *FFT* has been performed. In fact, the unsteady signal is assumed to have stationary behavior in each short time interval and a local Fourier spectrum is therefore calculated over this short interval.

From a mathematical point of view, a windowing operation of signal *f(t)* is realized in the time-frequency analysis by multiplying *f(t)* by a mobile window function $h(t-\tau)$, where τ is a variable parameter that represents the centre of the window support. The Short Time Fourier Transform (*STFT*) is defined in the following way:

$$\hat{F}_l(\omega,\tau) = \int_{-\infty}^{+\infty} f(t)\, h(t-\tau)\, e^{-j\omega t}\, dt \tag{18}$$

The position of the window in Eq. (18) can be shifted with respect to time by varying τ, and different Fourier spectra can then be obtained. Integrating Eq. (18) with respect to τ, one obtains

$$\hat{F}(\omega) = \int_{-\infty}^{+\infty} \hat{F}_l(\omega,\tau)\, d\tau = \int_{-\infty}^{+\infty} \left[\int_{-\infty}^{+\infty} f(t)\, h(t-\tau)\, d\tau \right] e^{-j\omega t}\, dt \tag{19}$$

Function $\hat{F}_l(\omega,\tau)$ represents a local Fourier transform, and the summation of all of the *STFT* over τ values ranging from $-\infty$ to $+\infty$ is equal to $\hat{F}(\omega)$. Since $\hat{F}(\omega)$ is the Fourier transform of a time convolution, it is given by the product of the Fourier transform of the signal, namely *F(ω)*, and the Fourier transform of the window, namely *H(ω)*:

$$\hat{F}(\omega) = F(\omega)\, H(\omega) \tag{20}$$

When the *STFT* is applied to the analysis of the time variations of a physical signal, the τ parameter in Eq. (18) is varied by finite steps of amplitude $\Delta\tau$. The higher the overlap period of two consecutive positions τ_i and $\tau_{i+1}=\tau_i+\Delta\tau$ of window *h* in the time domain, the more gradual the variation of the Fourier spectrum with respect to time. The extension of the time support ΔT_h of the window, i.e., the time interval in which the *h(t)* window is higher than zero, can be related to the sampling circular frequency (ω_s) and to the number of sampling points within the window support (*N*) by the relation $\Delta T_h=2\pi N/\omega_s$. The overlap period is equal to $\Delta t_{ov}=s\Delta T_h=2\pi n/\omega_s$, where *n* is the number of samplings in the overlap period Δt_{ov} and $s=n/N$ is the overlap factor. As a result, the temporal resolution of the *SFST* can be worked out as follows:

$$\Delta\tau = \Delta T_h - \Delta t_{ov} = \frac{2\pi}{\omega_s} N(1-s) \tag{21}$$

Both a reduction in *N* and an increase in *s* at fixed sampling frequency ω_s induces an improvement in the time resolution, that is, a diminution in $\Delta\tau$. The minimum value of $\Delta\tau$ is $2\pi/N$ and is reached for $s=N/(N-1)$.

A window function can be characterized in terms of its centre and its semiamplitude. The centre (t_0) and the semiamplitude (Δ_h) of a window function *h* are defined as

$$t_0 = \frac{1}{\|h\|_2}\int_{-\infty}^{+\infty} t\,|h(t)|^2\,dt \qquad \Delta_t = \frac{1}{\|h\|_2}\left[\int_{-\infty}^{+\infty}(t-t_0)^2|h(t)|^2\,dt\right]^{1/2} \tag{22}$$

where the norm $||h||_2$ represents the energy of the *h* function, which is given by

$$\|h\|_2 = \int_{-\infty}^{+\infty}|h(t)|^2\,dt \tag{23}$$

The definitions of centre and semiamplitude extend naturally to the frequency domain for the *H(ω)* function:

$$\omega_0 = \frac{1}{\|H\|_2}\int_{-\infty}^{+\infty}\omega\,|H(\omega)|^2\,d\omega \qquad \Delta_\omega = \frac{1}{\|H\|_2}\left[\int_{-\infty}^{+\infty}(\omega-\omega_0)^2|H(\omega)|^2\,d\omega\right]^{1/2} \tag{24}$$

where $\|H\|_2 = \int_{-\infty}^{+\infty}|H(\omega)|^2\,d\omega$.

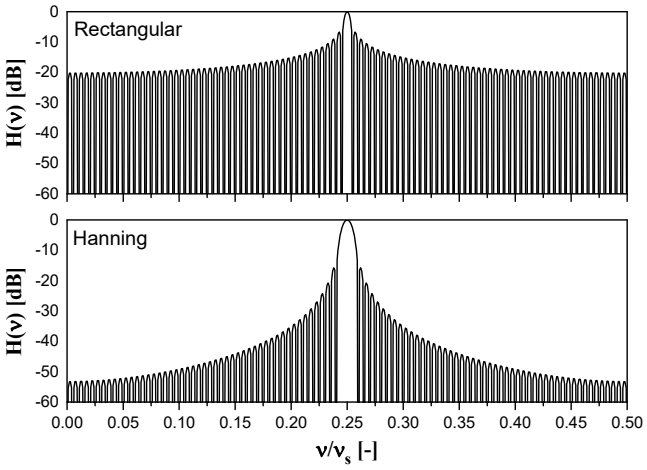

Figure 11. Different *h* functions and their Fourier transforms.

The selection of the optimum h window function is a central theme in the time frequency theory. Different shapes of window functions have been analyzed and tested by specialists in the field. Eq. (20) shows that the window modifies the frequency content of signal $f(t)$, which is given by $F(\omega)$. A rectangular shaped window (h_R, cf. Fig. 11) is a simple solution, but it is able to alter the spectrum of the original signal to a great extent. As an example, if $f(t)$ is a sinusoid with circular frequency $\omega=\omega_0$, the signal, which is windowed by means of a h_R function with its centre at ω_0, features a frequency spectrum that can be represented as a band centered on ω_0 (H_R is reported in Fig. 11) rather than as a single line at ω_0. Furthermore, the step transitions that occur in h_R generate high-frequency harmonic components in the $\hat{F}(\omega)$ spectrum. Other window functions have been proposed to partially solve these drawbacks of the rectangular window. One popular window function is the Hann filter (cf. h_H in Fig. 11), which is defined as follows (the here considered window has the center at point $n=(N-1)/2$):

$$h_H(n) = \frac{1}{2}\left[1-\cos\left(\frac{2\pi n}{N-1}\right)\right] \qquad 0 \le n \le N-1 \tag{25}$$

The h_H function goes to zero at $n=0$ and $n=N-1$, without any type of discontinuity, and therefore does not introduce any spurious high-frequency components in the frequency content of signal f. The Fourier spectrum of h_H, that is, H_H, has been illustrated in Fig. 11: a central lobe exists in the Fourier spectrum of the windowed function, with a higher extension than the corresponding one in the Fourier spectrum of the h_R windowed signal, but the number and the maximum values of the lateral lobes is reduced compared to the h_R case.

For any window function h, the amplitude of $H(\omega)$, i.e. $2\Delta_\omega$, increases as the amplitude of $h(t)$, i.e. $2\Delta_t$, reduces. The Heisenberg principle of indetermination governs the relationship between Δ_ω and Δ_t according to the following expression [37]:

$$\Delta_t \Delta_\omega \geq \frac{1}{2} \quad \Leftrightarrow \quad \Delta_t \Delta_\nu \geq \frac{1}{4\pi} \tag{26}$$

The two formulations are equivalent because $\nu=\omega/2\pi$ and hence $\Delta_\nu=\Delta_\omega/2\pi$. It is impossible, on the basis of these relations, to simultaneously reduce Δ_ω and Δ_t in order to obtain a high resolution of the unsteady signal $f(t)$ in either the time or the frequency domains. If the frequency resolution is improved, Δ_ω should be reduced, but this leads to an increase in Δ_t and therefore to a diminution in the capability of locating events in the time domain: phenomena that are closely coupled become difficult to distinguish. In the particular case of the *FFT*, the window function in Eq. (18) is $h_{FT}=1$, $\Delta_{t,FT}\to\infty$ while $\Delta_{\omega,FT}\to 0$ because H_{FT} is the Dirac delta function in the frequency domain: the description is therefore very accurate in the frequency domain, but it is impossible to localize the events with respect to time.

The Gaussian window, i.e., $h_G(n)=\exp\left\{-\frac{1}{2}\left[\frac{n-(N-1)/2}{\sigma(N-1)/2}\right]^2\right\}$, is the window function that minimizes the product between Δ_t and Δ_ω. In fact, it can be proved that the Gaussian window is the only function for which $\Delta_t\Delta_\omega=1/2$. When h_G is used in Eq. (18), the thus obtained $\hat{F}(\omega,\tau)$ is named the Gabor transform of the f function.

3.1 Spectrogram and mean instantaneous frequency numerical model

The time-frequency distribution related to signal $f(t)$ is a function $P_f(t,\nu)$, which is defined as follows [37]:

$$E_f = \int_{-\infty}^{+\infty}\int_{-\infty}^{+\infty} P_f(t,\nu)\,dt\,d\nu = \int_{-\infty}^{+\infty} |f(t)|^2\,dt \tag{27}$$

where E represents the energy of signal $f(t)$. The $P_f(t,\nu)$ distribution therefore represents an energy density function with respect to both time and frequency. The Parseval identity allows the energy of the signal to be calculated, starting from the knowledge of the Fourier spectrum ($F(\omega)$ or alternatively $F(\nu)$, which has been considered in what follows):

$$E_f = \int_{-\infty}^{+\infty} |f(t)|^2\,dt = \int_{-\infty}^{+\infty} |F(\nu)|^2\,d\nu \tag{28}$$

The marginal energy density functions of signal f are the density functions with respect to either t or ν. These functions are obtained by integrating $P_f(t,\nu)$ with respect to one of the independent variables:

$$M_f(\nu) = \int_{-\infty}^{+\infty} P_f(t,\nu)\,dt \qquad m_f(t) = \int_{-\infty}^{+\infty} P_f(t,\nu)\,d\nu \tag{29}$$

The marginal properties are said to hold when the following relations are satisfied:

$$|F(\nu)|^2 = \int_{-\infty}^{+\infty} P_f(t,\nu)\,dt \qquad |f(t)|^2 = \int_{-\infty}^{+\infty} P_f(t,\nu)\,d\nu \tag{30}$$

If the marginal properties are satisfied, Eqs. (27) and (28) are automatically verified, but the opposite is generally not true. Therefore, the marginal properties represent a more severe requirement than Eqs. (27) and (28).

The time-frequency distribution can be interpreted as a density probability function and has been used in the simulation code to calculate the mean instantaneous frequency $\bar{\nu}(t)$ according to the following formula [37]:

$$\bar{\nu}(t) = \frac{1}{\int_{-\infty}^{+\infty} P_f(t,\nu)\,d\nu} \int_{-\infty}^{+\infty} \nu\, P_f(t,\nu)\,d\nu \tag{31}$$

Eq. (31) gives the baseline harmonic contribution to signal *f(t)* at each time instant and is a fundamental relation for many engineering applications. The spectrogram $P_{sp}(t,\nu)$ is the square modulus of $\hat{F}_l(\omega,\tau)$ and has been selected as the time-frequency distribution in the developed code:

$$P_{sp}(t,\nu) = \left[\int_{-\infty}^{+\infty} f(\tau) h(\tau - t) e^{-j2\pi\nu\tau} d\tau \right]^2 = \hat{F}_l(\omega,\tau)^2 \tag{32}$$

Function P_{sp} gives the energy density with respect to time and frequency of the $f(t)h(t-\tau)$ windowed signal. In fact, the following relation holds:

$$\begin{aligned} &\int_{-\infty}^{+\infty} P_{sp}(t,\nu)\,d\nu = \int_{-\infty}^{+\infty} \left\{ \left[\int_{-\infty}^{+\infty} f(\tau) h(\tau - t) e^{-j2\pi\nu\tau} d\tau \right] \left[\int_{-\infty}^{+\infty} f^*(\tau') h^*(\tau' - t) e^{j2\pi\nu\tau'} d\tau' \right] \right\} d\nu = \\ &= \int_{-\infty}^{+\infty} e^{-j2\pi\nu(\tau-\tau')} d\nu \int_{-\infty}^{+\infty} \int_{-\infty}^{+\infty} \left[f(\tau) f^*(\tau') h(\tau - t) h^*(\tau' - t) e^{-j2\pi\nu\tau} \right] d\tau\, d\tau' \end{aligned} \tag{33}$$

where f^* and h^* are the complex conjugates of functions f and h, respectively. Furthermore, since the representation of the Dirac delta function in the frequency domain is generally given by

$$\delta(t) = \frac{1}{2\pi} \int_{-\infty}^{+\infty} e^{j\omega t} d\omega = \int_{-\infty}^{+\infty} e^{j2\pi\nu t} d\nu \tag{34}$$

it is possible to obtain:

$$\begin{aligned} &\int_{-\infty}^{+\infty} P_{sp}(t,\nu)\,d\nu = \int_{-\infty}^{+\infty} \int_{-\infty}^{+\infty} \left[f(\tau) f^*(\tau') h(\tau - t)\, h^*(\tau' - t) \delta(\tau' - \tau) \right] d\tau\, d\tau' = \\ &= \int_{-\infty}^{+\infty} |f(\tau)|^2 |h(\tau - t)|^2 d\tau \neq |f(t)|^2 \end{aligned} \tag{35}$$

Finally, by developing a symmetric procedure for quantity $\int_{-\infty}^{+\infty} P_{sp}(t,\nu)\,dt$, the following expression can be obtained:

$$\int_{-\infty}^{+\infty} P_{sp}(t,\nu)\,dt = \int_{-\infty}^{+\infty} |F(\nu')|^2 |H(\nu' - \nu)|^2 d\nu' \neq |F(\nu)|^2 \tag{36}$$

The marginal properties are not verified by Eqs. (36) and (35); they could be satisfied if $h(\tau-t)=\delta(\tau-t)$ and $H(\nu'-\nu)=\delta(\nu'-\nu)$ simultaneously, but, on the basis of the Heisenberg principle, this is not possible. In other words, the windowing operation alters the signal and leads to spurious contributions, due to the square of $|h|$ and $|H|$. This is why the integrals of $P_{sp,}$ with respect to t or ν, are not equal to $|F(\nu)|^2$ and $|f(t)|^2$, respectively. However, if $\int_{-\infty}^{+\infty}|h(\tau-t)|^2 d\tau=1$, integral $\int_{-\infty}^{+\infty}\int_{-\infty}^{+\infty}P_{sp}(t,\nu)\,dt\,d\nu$ becomes equal to energy E of signal $f(t)$, and the spectrogram can therefore be confirmed to be a feasible choice for the $P_f(t,\nu)$ function in Eq. (31) because it does not alter the energy of the signal, although the marginal properties are not satisfied.

Eqs. (18), (21)-(25), (31) (32), together with energy consistency condition $\int_{-\infty}^{+\infty}|h_H(\tau-t)|^2 d\tau=1$, which makes Eqs. (27) and (28) hold, have been implemented in the developed Matlab numerical tool to perform the combustion time frequency analyses. In this code, $f(t)$ can be either the in-cylinder pressure signal $p(t)$ or the pressure difference basis of a preliminary campaign of *STFT* tests on $p(t)$: N=50, s=0.96, ω_s=120 kHz and, from Eq. (21), $\Delta\tau\approx$170 μs.

3.2 Diesel combustion characterization by means of time-frequency analysis.

Figures 12, 14, 16 and 17 plot the injected mass flow-rate (G_{inj}), the cylinder pressure (in the upper part), the *HRR*, the x_b and the mean instantaneous frequency crankshaft angle-based distributions (in the bottom part) at different engine working conditions for the same diesel engine layout to which Figs. 8-10 refer. Besides, Figs. 13 and 15 report the 3D graphs of spectrogram P_{sp}, normalized to its maximum value, for two distinct engine working conditions; P_{sp} has been calculated by means of Eq. (32), in which $f:=p$, $h:=h_H$ and t is replaced by θ. The plotted G_{inj} data were measured at the hydraulic rig, in the absence of combustion, under the same injector working conditions as those of the engine tests, whereas the cylinder pressure time histories were measured in the engine at the dynamometer cell. The *HRR* and the x_b plotted traces have been calculated by means of a three-zone diesel combustion model on the basis of the measured p and G_{inj} histories. It is worth observing that the measured G_{inj} can differ significantly from the actual injected flow-rate time history measured at the dynamometer cell, especially for small injection events, because the temperature levels of the fuel are much higher at the dynamometer cell than at the hydraulic test rig. Finally, the mean instantaneous frequency has been evaluated through Eq. (31), in which function $f(t)$ has been replaced by $p(\theta)$. The reported diagrams allow the pattern of the $\bar{\nu}(\theta)$ signal to be interpreted on the basis of the other physical variable distributions according to a learning procedure.

Figures 12 and 13 refer to a pilot-main injection schedule (two injection pulses are present in the G_{inj} trace) performed at *bmep*=500 kPa and n=2000 rpm. Fig. 13 shows that P_{sp} is only higher than zero in the 320°÷450° *CA* θ range. Furthermore,

489 the spectrogram indicates that the frequency content of the considered combustion event is lower than 4 kHz. In Fig. 12,
490 the first maximum point (P_1), which occurs along the $\bar{v}(\theta)$ distribution, is caused by the injection of fuel into the
491 combustion chamber. The subsequent decrease in $\bar{v}$ can be ascribed to fuel evaporation and the *SOC* is located in
492 correspondence to the minimum P_2 point. The possible discrepancies between the phasing of P_2 and the beginning of the
493 *HRR* trace can be ascribed to the inaccuracy of the combustion model when simulating the start of combustion. The time
494 frequency analysis can therefore also be applied to validate and possibly improve the prediction capability of combustion
495 diagnostic tools. The increase in $\bar{v}$, which is detected after P_2, is a consequence of the combustion development. A first,
496 more pronounced peak, related to the premixed combustion phase of the pilot injection, can be detected (P_3) and this is
497 followed by a second one (P_4), which is due to a smaller, late combustion event related to the pilot injected fuel. The
498 intensity of the P_4 peak is also reduced because the piston has already started its downstroke after *TDC*; if this phenomenon
499 is taken into account, the late combustion event of the pilot injected fuel seems to be underestimated in the *HRR* trace
500 obtained when the model is used.

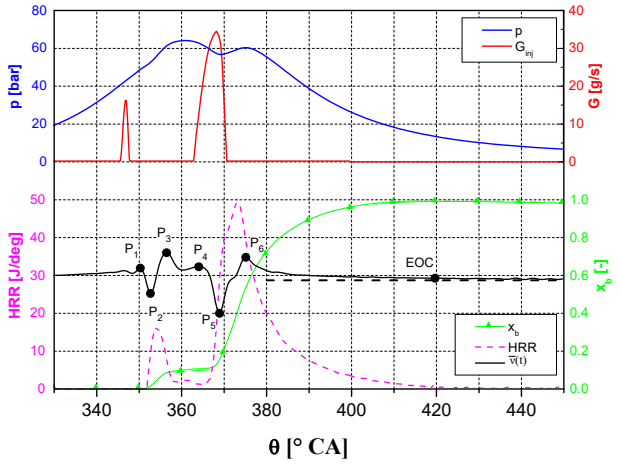

Figure 12. Time frequency analysis

(diesel engine, *bmep*=500 kPa, *n*=2000 rpm).

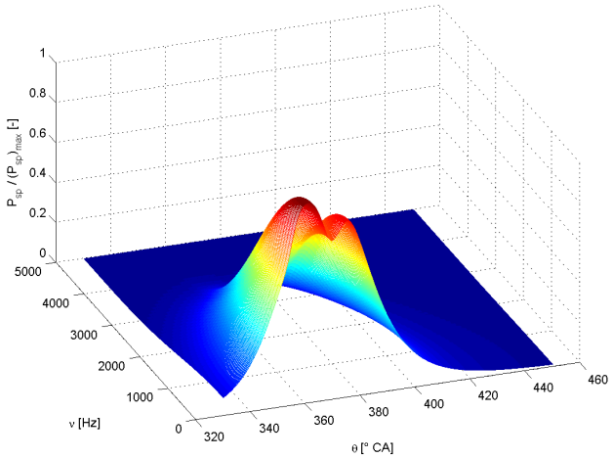

Figure 13. Normalized spectrogram of *p*

(diesel engine, *bmep*=500 kPa, *n*=2000 rpm).

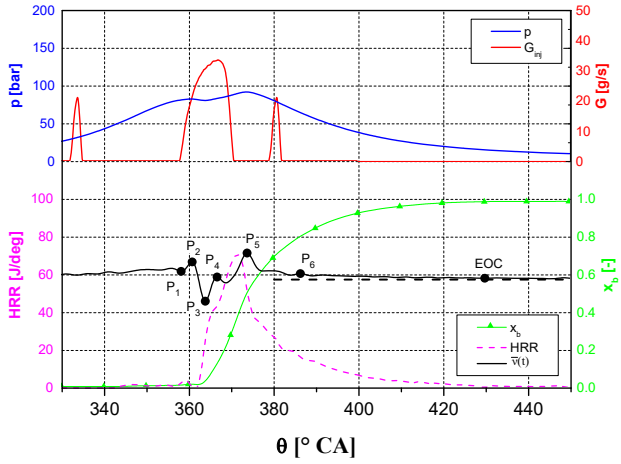

Figure 14. Time frequency analysis of *p*

(diesel engine, *bmep*=800 kPa, *n*=2500 rpm).

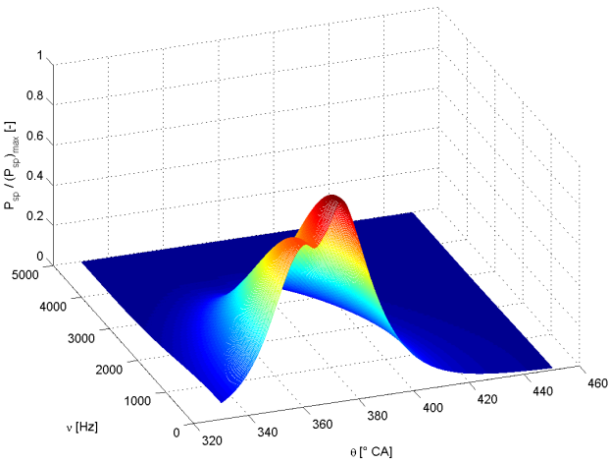

Figure 15. Normalized spectrogram of *p*

(diesel engine, *bmep*=800 kPa, *n*=2500 rpm).

The diminution in the $\bar{v}$ values, which occurs within the 365÷368°*CA* θ range, is induced by the evaporation of the main injected fuel and by the combustion chamber expansion due to the piston downstroke. The *SOC* of the main injected fuel is placed at about θ≈368°*CA,* and a minimum point (P_5) can be observed in the $\bar{v}$ curve. The consequent $\bar{v}$ increase is characterized by the presence of two phases: a first phase (up to 375°*CA*), in which the frequency grows at a higher rate, and a second phase (from 375°*CA* to P_6), in which the slope of ν with respect to θ becomes lower. It can be stated, on the basis of the *HRR* trace, that the former phase is related to the premixed combustion of the main injected fuel and the latter phase refers to its diffusive combustion regime. The *EOC* is evaluated as the time instant at which the $\bar{v}$ curve matches a horizontal line, which is represented by a dashed horizontal line in Figs 14-17. The *EOC* prediction of the time frequency analysis is physically consistent with the pattern of the x_b and *HRR* curves at that angle.

Figs 14 and 15 refer to *bmep*=800 kPa and *n*=2500 rpm under a pilot-main-after triple injection schedule (cf. the G_{inj} trace). In Fig. 14, the *SOC* of the pilot injection occurs at P_1, which represents the minimum just before the first distinct

maximum; the increase in the mean instantaneous frequency, due to pilot combustion, is soon overbalanced by both the cylinder volume expansion after *TDC* and by the evaporation of the main injected fuel; a maximum point of $\bar{\nu}$ therefore occurs in P_2. The following minimum $\bar{\nu}$ point, i.e. P_3, indicates the beginning of the main combustion after the evaporation of part of the fuel injected in the main pulse; the P_4 peak is related to the premixed combustion part of the main injected fuel and also to a possible residual pilot combustion, whereas P_5 refers to the diffusive combustion of the main injected fuel and corresponds to a slope variation in the *HRR* trace. Furthermore, the after-injection causes peak P_6 in the $\bar{\nu}$ distribution (also perceivable in the *HRR* trace) and, finally, the $\bar{\nu}$ curve becomes almost horizontal at θ≈430°*CA,* where the *HRR* trace is practically null. Fig. 15 reports the 3D spectrogram that corresponds to the data in Fig. 14: two bumps can be noticed in the $P_{sp}(\nu, t)$ graph, as in Fig. 13, even though the number of injection shots is different (three shots in Fig. 15 and two shots in Fig. 13). In both cases, the earlier peak corresponds to the piston at *TDC* (it has been verified that this peak is also present in the spectrogram of the motored pressure), while the other bump is phased with the main combustion *HRR* peak.

Figure 16 reports a pilot-pilot-main injection case at *bmep*=200 kPa and *n*=1500 rpm. The closest-to-main pilot injection is referred to as pilot 1, whereas the more distant pilot injection is referred to as pilot 2. Since the timing of the pilot 2 injection occurs early during the piston compression stroke, the pilot 2 injected fuel exhibits a two-stage ignition: the *HRR* dashed curve becomes different from zero at θ≈350°*CA*, but the sharp increase in *HRR* occurs later, at θ≈356°*CA.* Correspondingly, in the curve of the mean instantaneous frequency, P_2 and P_3 are the *SOC* and the maximum $\bar{\nu}$ point related to the cool flames, whereas P_4 and P_5 (related to the first peak in the *HRR* trace) are analogous to P_2 and P_3 for the hot flames. The pilot 1 *SOC* is phased with P_6, while P_7 represents the maximum $\bar{\nu}$ point due to pilot 1 combustion and is related to the second peak in the *HRR* trace. The *SOC* of the main injected fuel occurs at P_8, and the development of the main combustion leads to P_9, which is related to the third and maximum peak in *HRR*. The end of combustion occurs at θ≈420°*CA,* an angle at which both *HRR* and x_b are practically constant.

Finally, Fig. 17 refers to a pilot-pilot-main-after quadruple injection event (*bmep*=500 kPa and *n*=1500 rpm). Even though the overall combustion evolution is complex and rich in events, the mean instantaneous frequency distribution allows the main features of the different combustion events to be identified. The *SOC* of the pilot 2, pilot 1 and main injected fuel quantities are phased with P_1, P_3 and P_6, respectively, and related to the local minima of the $\bar{\nu}$ curve. The local maximum P_2 refers to pilot 2 combustion, while P_4 is related to both the pilot 2 and pilot 1 injected fuel masses (part of the pilot 2 injected fuel burns together with the pilot 1 injected fuel) and P_5 concerns a late combustion event of the pilot 1 injected fuel. The local maxima P_7 and P_8 of the $\bar{\nu}$-θ distribution correspond, respectively, to a premixed phase of the main

combustion and to a diffusive phase of both the main combustion and after combustion. The after combustion is responsible for the weak decrease in $\bar{v}$ that occurs after $P_{8,}$ and the *EOC* is located close to $\theta \approx 400°CA$.

The time frequency analysis can also be applied to the difference, $\Delta p_{comb,}$ between $p(\theta)$ and motored pressure $p_{mot}(\theta)$ instead of to the $p(\theta)$ signal. This is justified by the fact that $\Delta p_{comb}(\theta)$ roughly represents the $p(\theta)$ portion, which should be more closely related to the combustion events, whereas $p_{mot}(\theta)$ is closely related to the chamber volume variation that is due to piston motion. Figs. 18 and 19 report $\bar{v}$ calculated on the basis of Δp_{comb} ($f := \Delta p_{comb}$ in spectrogram P_{sp}) for the same engine working conditions as Figs. 14 and 17, respectively. The main advantages of the time frequency analysis applied to Δp_{comb} are the amplification of the peaks in the $\bar{v}$ distribution and a general reduced uncertainty in the determination of *EOC,* compared to the p analysis. In fact, the θ value at which the $\bar{v}$ curve matches the horizontal line pattern at the end of combustion results to be more clearly identified for the Δp_{comb} case than for the p case. On the other hand, the knowledge of the motored pressure time history is required for the calculus of $\Delta p_{comb}(\theta)$. However, the determination of *SOC* is always easier, and virtually corresponds to the crank angle at which $p\ (\theta)$ and $p_{mot}(\theta)$ start to differ, whereas the two pressure traces will never result in the same values when combustion extinguishes because $p\ (\theta)$ will always remain higher. In addition, the suitable $p_{mot}(\theta)$ signal cannot be experimentally measured in a turbocharged engine. In fact, because of the difference in intake manifold pressure between firing and motoring tests, the Δp_{comb} signal, obtained as the difference between the experimental measurements of $p\ (\theta)$ and $p_{mot}(\theta)$, would be higher than zero before *SOC*. Therefore, in the case of turbocharged engines, the proper motored trace, which is useful for the Δp_{comb} calculus, has to be calculated starting from a firing cycle and considering a polytropic evolution from an angular position where combustion has not yet started. Finally, by comparing Fig 14 with Fig. 18 and Fig 17. with Fig 19, it can be observed that the trends of the mean instantaneous frequency distributions pertaining to $p(\theta)$ and Δp_{comb} are really quite similar.

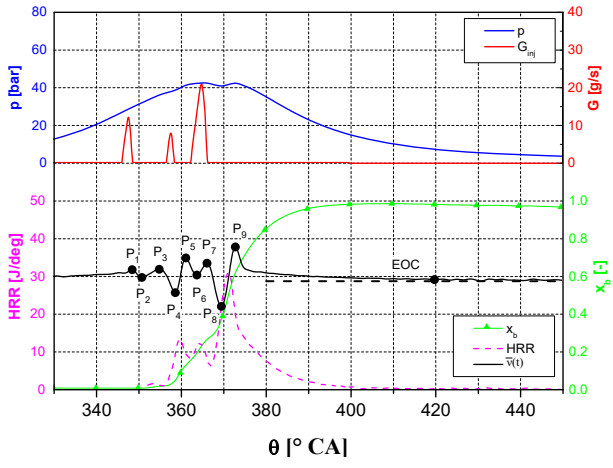

Figure 16. Time frequency analysis of *p*

(diesel engine, *bmep*=200 kPa, *n*=1500 rpm).

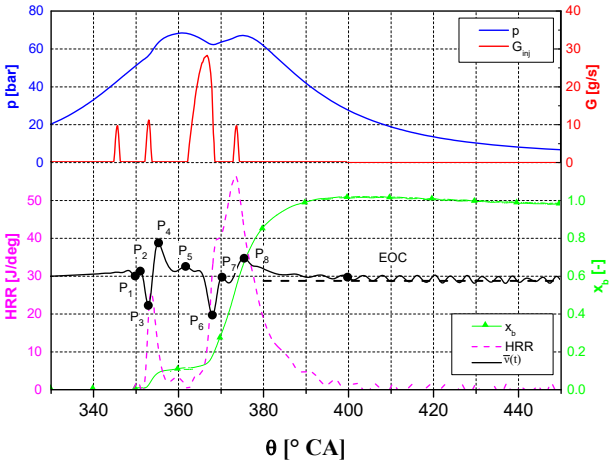

Figure 17. Time frequency ana

(diesel engine, *bmep*=500 kPa, *n*=

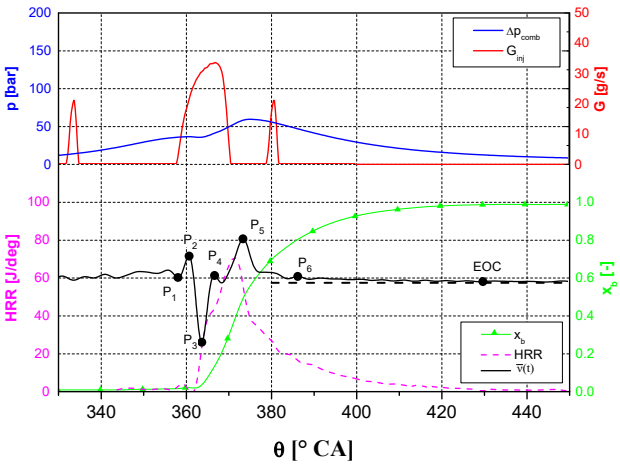

Figure 18. Time frequency analysis of Δp_{comb} (diesel engine, *bmep*=800 kPa, *n*=2500 rpm).

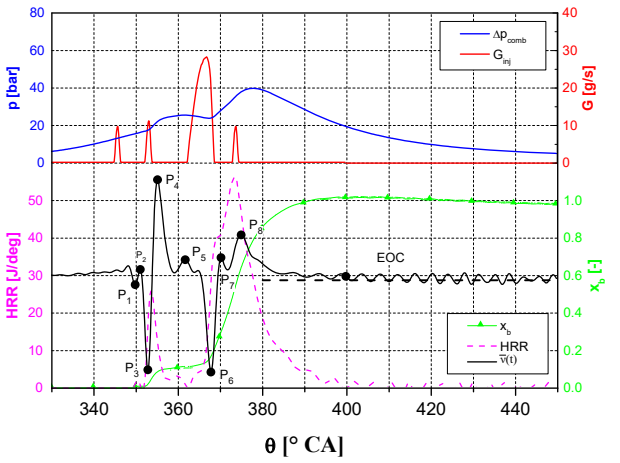

Figure 19. Time frequency analys (diesel engine, *bmep*=500 kPa, *n*=

561

562 4. CONCLUSIONS.

563 The most popular in-cylinder pressure-based direct techniques have been analyzed mathematically, and the hypotheses
564 on which each technique is founded have been pointed out. Different typologies of engines, i.e., gasoline, methane and
565 diesel engines, and different *bmep* and *n* working conditions have been considered in order to perform a significant
566 comparison of the tested pressure-based direct methods. The predictions obtained using these methods have been
567 compared with the numerical outcomes of two-zone and three-zone combustion models of spark-ignition and
568 compression-ignition engines, respectively.

569 The start and end of combustion, for spark ignition engines fuelled with either gasoline or methane, are generally
570 identified with satisfactory precision by the pressure-based methods. The simulation of the burned mass fraction time
571 history is also accurate: the best performance has been achieved with the *MLK* procedure, which accurately reproduces
572 the x_b traces obtained with the two-zone combustion model, but the *PMR* technique also provides very satisfactory results.
573 In particular, the *PMR* and *MLK* procedures have been proved to be based on the same physical law and this justifies the
574 very similar performance that is obtained when these methods are used.

575 As far as diesel combustion is concerned, the accuracy of the pressure-based direct techniques in the prediction of *SOC*,
576 *EOC* and the x_b trace generally deteriorates, compared to spark-ignition engines, and the results can become worse as the
577 number of injections increases, because the combustion evolution is more complex, and more sophisticated approaches
578 are required. The only acceptable technique has proved to be the *PDR* method: both the *SOC* and the *EOC* can be evaluated

with adequate accuracy for single and double injection strategies. On the other hand, an accurate prediction of the burned mass time history with pressure-based direct techniques seems to be impracticable for diesel engines.

The time frequency analysis of the in-cylinder pressure, in spite of not being able to provide a complete x_b curve, represents a useful means of investigation for diesel engines because it can offer a great deal of information on the combustion evolution as well as on the initial and final instants of the overall process. A home-made numerical tool has been developed to perform *STFT* tests on the in-cylinder pressure. The mean instantaneous frequency versus crankshaft angle distribution, which is obtained from the spectrogram of the in-cylinder pressure, allows the *SOC*, the fuel evaporation phase and the combustion stage pertaining to each injection shot to be identified clearly. Furthermore, the ignition delays of both cool and hot flames as well as the timings of both premixed and diffusive combustion can be localized accurately during the piston compression and expansion strokes.

The application of the time frequency analysis to the pressure difference between the in-cylinder pressure and the motored pressure leads to better results than in the case of the in-cylinder pressure signal. In particular, it leads to amplified peaks in the $\bar{v}$ distribution and to less uncertainty in the determination of *EOC* than in the case of the in-cylinder pressure.

5. NOMENCLATURE.

bmep	brake mean effective pressure
BDC	bottom dead center
c	constant specific heat of the polytropic evolution
c_v	specific heat at constant volume
dp/dt	pressure derivative with respect to time
E	energy of the signal
EOC	end of combustion
f(t)	time function
F(ω)	Fourier transform of function *f*
FFT	fast Fourier transform
$\hat{F}_l(\omega,\tau)$	short time Fourier transform
$\hat{F}(\omega)$	integral of the short time Fourier transform with respect to time
FPR	final pressure ratio
G_{inj}	injected mass flow-rate
h(t)	window function

608	$H(\omega)$	Fourier transform of the window function
609	*imep*	indicated mean effective pressure
610	*iV*	engine displacement
611	τ	parameter that defines the position of the window function in the time domain
612	H_i	lower heating value
613	*HRR*	heat release rate
614	*IC*	internal combustion engines
615	*m*	marginal function in the time domain; polytropic exponent
616	m_b	mass of burned fuel
617	$m_{b,tot}$	total mass of burned fuel
618	m_c, m_e	exponents of the polytropic compression and expansion phases
619	*M*	mass of the burning mixture; marginal function in the frequency domain
620	*MFB50*	angle at which 50% of the combustion mixture has burned
621	*MLK*	McCuiston, Lavoie and Kaufmann (procedure)
622	*MPR*	modified pressure ratio
623	*n*	engine speed; number of points in the overlap zone during the shift of the window function
624	*N*	number of intervals in the combustion process; number of points of the window function
625	*P*	time-frequency distribution function
626	$P_1 \div P_9$	noteworthy points along the mean instantaneous frequency time distribution
627	P_{sp}	spectrogram
628	*p*	in-cylinder instantaneous pressure
629	*PDR*	pressure departure ratio (algorithm)
630	*PR*	pressure ratio
631	*PRM*	pressure ratio management (procedure)
632	*R*	elastic constant of the gas
633	*RW*	Rassweiler and Withrow (procedure)
634	*SOC*	start of combustion
635	*STFT*	short time Fourier transform
636	*t*	time
637	t_0	center of the window function in the time domain
638	*TDC*	top dead center

639	v	specific volume
640	V	instantaneous volume of the combustion chamber
641	x_b	burned gas mass fraction
642	y	dimensionless quantity in the *MLK* algorithm
643	γ	ratio between the principal specific heats
644	$\delta(t)$	Dirac delta function
645	δq	heat per unit mass
646	δQ	heat
647	Δ_t	amplitude of the window function in the time domain
648	Δ_ν	amplitude of the window function in the frequency domain
649	Δ_ω	amplitude of the window function in the circular frequency domain
650	Δp	pressure difference
651	ΔT	temperature difference
652	ΔT_h	time support of the window function
653	Δt_{ov}	overlap time interval between consecutive window function positions
654	$\Delta\tau$	time resolution of the short time Fourier transform
655	$\Delta\theta$	crankshaft angle increment
656	ν	frequency
657	$\bar{\nu}(t)$	mean instantaneous frequency
658	θ	crankshaft angle
659	Θ	overall duration
660	ω	circular frequency
661	ω_0	center of the window function in the circular frequency domain
662	ω_s	sampling circular frequency
663		
664	*Subscripts*	
665	*ahrr*	apparent heat release rate
666	*comb*	combustion
667	*EOC*	at end of combustion
668	*f*	relative to function *f*

hrr	heat release rate
ht	heat transfer
max	maximum
mot	motored
SOC	at start of combustion
TDC	corresponding to top dead center

6. REFERENCES.

[1] Kuratle, R. and Märki, B. Influencing Parameters and Error Sources During Indication on Internal Combustion Engines. SAE Technical Paper 920233, 1992, doi:10.4271/920233.

[2] Gatowski JA, Balles EN, Chun KM., Nelson FE. Ekchian JA and Heywood JB, Heat Release Analysis of Engine Pressure Data. SAE Technical Paper 841359, 1984, doi:10.4271/841359.

[3] Galloni E. Dynamic knock detection and quantification in a spark ignition engine by means of a pressure based method", *Energy Conversion and Management*, 64 (2012), pp. 256-262.

[4] Carlucci AP, Laforgia D, Motz S, Saracino R, Wenzel SP. Advanced closed loop combustion control of a LTC diesel engine based on in-cylinder pressure signals. *Energy Conversion and Management*, 77 (2014), pp. 193-207.

[5] Desantes JM, Galindo J, Guardiola C, Dolz V. Air mass flow estimation in turbocharged diesel engines from in-cylinder pressure measurement. *Experimental Thermal and Fluid Science*, 34 (2010), pp. 37-47.

[6] Payri F, Olmeda P, Guardiola C, Martin J. Adaptive determination of cut-off frequencies for filtering the in-cylinder pressure in diesel engines combustion analysis. *Applied Thermal Engineering*, 31 (2011), pp. 2869-2876.

[7] Chung J, Oh S, Min K, Sunwoo M. Real-time combustion parameter estimation algorithm for light-duty diesel engines using in-cylinder pressure measurement. *Applied Thermal Engineering* 60 (2013) 33-43.

[8] Antonopoulos AK, Hountalas DT. Effect of instantaneous rotational speed on the analysis of measured diesel engine cylinder pressure data. *Energy Conversion and Management*, 60 (2012), pp. 87-95.

[9] Rocco V. Dynamic T.D.C. and Thermodynamic Loss Angle Measurement in a D. I. Diesel Engine. SAE Technical Paper 851546, 1985, doi:10.4271/851546.

[10] Rocco V. D.I. Diesel Engine In-Cylinder Pressure Data Analysis Under T.D.C. Setting Error. SAE Technical Paper 930595, 1993, doi:10.4271/930595.

[11] Brunt MFJ and Emtage AL. Evaluation of Burn Rate Routines and Analysis Errors. SAE Technical Paper 970037, 1997, doi:10.4271/970037.

[12] Bueno AV, Velasquez JA, Milanez LF. A new engine indicating measurement procedure for combustion heat release analysis. *Applied Thermal Engineering* 29 (2009) 1657–1675, doi:10.1016/j.applthermaleng.2008.07.023.

[13] Lujan JM, Bermudez V, Guardiola C, Abbad A. A methodology for combustion detection in diesel engines through in-cylinder pressure derivative signal. *Mechanical Systems and Signal Processing* 24 (2010) 2261–2275, doi:10.1016/j.ymssp.2009.12.012.

[14] Savva NS, Hountalas DT. Evolution and application of a pseudo-multi-zone model for the prediction of NOx emissions from large-scale diesel engines at various operating conditions. *Energy Conversion and Management*, 85 (2014), pp. 373-388.

[15] Rakopoulos CD, Michos CN. Development and validation of a multi-zone combustion model for performance and nitric oxide formation in syngas fueled spark ignition engine. *Energy Conversion and Management* 49 (2008) 2924–2938.

[16] Marvin CF. Combustion time in the engine cylinder and its effects on engine performance. *NACA Tech Report 276*, 1927.

[17] Heywood JB. Internal combustion engine fundamentals. New York: McGraw-Hill; 1988.

[18] Shehata MS. Cylinder pressure, performance parameters, heat release, specific heats ratio and duration of combustion for spark ignition engine. *Energy*, 35(12) (2010), pp. 4710-4725.

[19] Rassweiler GM and Withrow L. Motion Pictures of Engine Flames Correlated with Pressure Cards. SAE Technical Paper 380139, 1938, doi:10.4271/380139.

[20] Brunt MFJ, Rai H and Emtage AL. The Calculation of Heat Release Energy from Engine Cylinder Pressure Data. SAE Technical Paper 981052, 1998, doi:10.4271/981052.

[21] McCuiston FD, Lavoie GA and Kauffmann CW. Validation of a Turbulent Flame Propagation Model for a Spark Ignition Engine. *SAE Transactions*, vol. 86 (1977), pp. 200-223.

[22] Krieger RB and Borman GL. The computation of apparent heat release for internal combustion engines. ASME paper 66-WA/DGP-4 in Proc. Diesel Gas Power, ASME, 1966.

[23] Hohenberg GF. Advanced Approaches for Heat Transfer Calculations. SAE Technical Paper 790825, 1979, doi:10.4271/790825.

[24] Woschni GA. Universally Applicable Equation for the Instantaneous Heat Transfer Coefficient in the Internal Combustion Engine. SAE Technical Paper 670931, 1967, doi:10.4271/670931.

[25] Guezennec Y and Hamama W. Two-Zone Heat Release Analysis of Combustion Data and Calibration of Heat Transfer Correlation in an I. C. Engine. SAE Technical Paper 1999-01-0218, 1999, doi:10.4271/1999-01-0218.

[26] Finesso R and Spessa E. A real time zero-dimensional diagnostic model for the calculation of in-cylinder temperatures, HRR and nitrogen oxides in diesel engines. *Energy Conversion and Management*, 79 (2014), pp. 498-510.

730 [27] Baratta M, d'Ambrosio S, Spessa E, Vassallo A. Cycle-resolved detection of combustion start in SI engines by
731 means of Different in-cylinder pressure data reduction techniques. In: Spring technical conference of the ASME
732 internal combustion engine division; 2006.
733 [28] Baratta M, d'Ambrosio S, Spessa E, Vassallo A. Analysis of cyclic variability in a Bi-fuel engine by means of a
734 'cycle-resolved' diagnostic technique. In: Fall technical conference of the ASME ICED; 2005.
735 [29] Bayraktar H. Theoretical investigation of flame propagation process in an SI engine running on gasoline–ethanol
736 blends. *Renewable Energy* 32 (2007) 758–771.
737 [30] Thurnheer T, Soltic P. The polytropic volume method to detect engine events based on the measured cylinder
738 pressure. *Control Engineering Practice* 20 (2012) 293–299. doi:10.1016/j.conengprac.2011.11.005.
739 [31] Ball JK, Raine RR, Stone CR. Combustion analysis and cycle-by-cycle variations in spark ignition engine
740 combustion - Part 1: an evaluation of combustion analysis routines by reference to model data. *Proc. Instn Mech.*
741 *Engrs*, *Part D*, *Journal of Automobile Engineering*, Vol 212, 381-399, 1998. DOI: 10.1243/0954407981526046
742 [32] Asad U, Zheng M. Fast heat release characterization of a diesel engine. *International Journal of Thermal Sciences*
743 47 (2008) 1688–1700. doi:10.1016/j.ijthermalsci.2008.01.009.
744 [33] Irimescu A, Marchitto L, Merola SS, Tornatore C, Valentino G. Evaluation of different methods for combined
745 thermodynamic and optical analysis of combustion in spark ignition engines. *Energy Conversion and Management*,
746 87 (2014), pp. 914-927.
747 [34] Baratta M, Misul D. Development and assessment of a new methodology for end of combustion detection and its
748 application to cycle resolved heat release analysis in IC engines. *Applied Energy* 98 (2012) 174–189.
749 http://dx.doi.org/10.1016/j.apenergy.2012.03.020.
750 [35] Payri F, Luján JM, Guardiola C, Rizzoni G. Injection diagnosis through common-rail pressure measurement. *Proc.*
751 *Instn Mech. Engrs, Part D, Journal of Automobile Engineering*, Vol 220, 347-357, 2006. DOI:
752 10.1243/09544070JAUTO34.
753 [36] Samimy B, Rizzoni G. Engine Knock Analysis and Detection Using Time-Frequency Analysis. SAE Technical
754 Paper 960618, 1996, doi:10.4271/960618.
755 [37] Cohen L. Time-Frequency Signal Analysis. McGraw Hill, 1995.
756 [38] Feng Z, Liang M, Chu F. Recent advances in time-frequency analysis methods for machinery fault diagnosis: a
757 review with application examples. *Mechanical Systems and Signal Processing*, 38 (2013), pp. 165-205.
758 [39] Stankovic L, Djurovic I, Stankovic S, Simeunovic M, Djukanovic S, and Dakovic M. Instantaneous frequency in
759 time-frequency analysis; enhanced concepts and performance of estimation algorithms. *Digital Signal Processing*,
760 35 (2014), pp. 1-13.

761 [40] Catania AE, d'Ambrosio S, Mittica A and Spessa E. Experimental investigation of fuel consumption and exhaust
762 emissionsof a 16V pent-roof engine fueled by gasoline and CNG. SAE Technical Paper No. 2001-01-1191.
763 [41] Harrington JA. Application of a new combustion analysis method in the study of alternate fuel combustion and
764 emission characteristics. Symposium on Future Automotive Fuels, 1975, GM Research Lab, Michigan, USA.
765 [42] Sellnau M, Matekunas FA, Battiston PA, Chang CF, Lancaster DR. Cylinder-Pressure-Based Engine Control Using
766 Pressure-Ratio-Management and Low-Cost Non-Intrusive Cylinder Pressure Sensors. SAE Technical Paper No.
767 2000-01-0932.
768 [43] d'Ambrosio S, Spessa E, Vassallo A, Ferrera M, Peletto C. Experimental investigation of fuel consumption, exhaust
769 emissions and heat release of a small-displacement turbocharged *CNG* engine. SAE Technical Paper 2006-01-0049.
770 [44] d'Ambrosio S, and Ferrari A. Potential of multiple injection strategies in improvement of diesel engine emissions
771 and performance. Part 1: double pilot injection. Submitted to *Applied Energy* for publication.